Case Studies in Thermal Engineering 79 (2026) 107774

Contents lists available at ScienceDirect

Case Studies in Thermal Engineering

journal homepage: www.elsevier.com/locate/csite

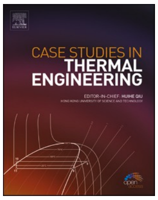

Thermal performance assessment of spacer-filled air-gap membrane distillation systems with varying saline feeds

Alaa Adel Ibrahim [*], Iurii Dolganov, Stephan Leyer

Department of Engineering, University of Luxembourg, 6 Rue Richard Coudenhove-Kalergi, Kirchberg, 1359, Luxembourg

GRAPHICAL ABSTRACT

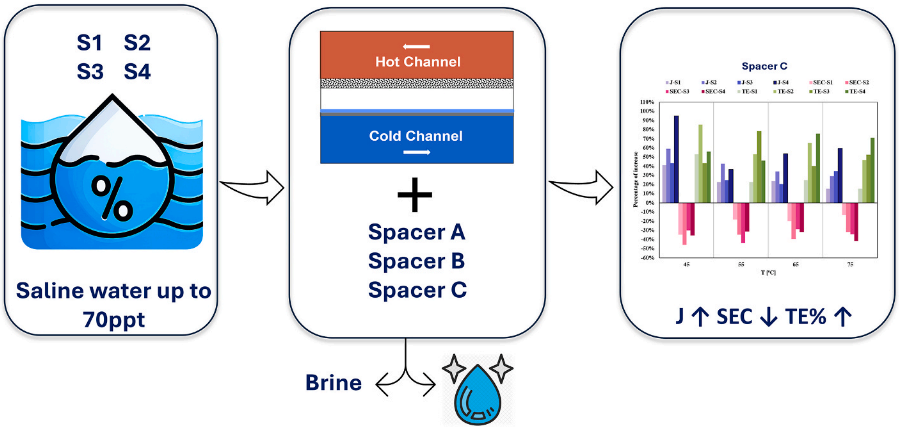

ARTICLE INFO

Keywords:
AGMD
Thermal performance
Seawater
Brackish water
Hypersaline water
Energy consumption
Permeate flux

ABSTRACT

Air gap membrane distillation (AGMD) represents a promising technology for seawater desalination, yet performance limitations associated with temperature polarization and inadequate flow dynamics present significant obstacles. Feed channel spacers constitute a proven strategy for mitigating polarization and fouling through enhanced fluid mixing and turbulence generation, thereby improving transport phenomena and permeate productivity. This work presents three novel spacer designs (Mix-1, Mix-2, and Spiral), developed based on industrial mixing principles to promote enhanced flow mixing and consequently improve mass and heat transfer mechanisms within the feed channel. Comprehensive experimental evaluation was conducted using a

---

[*] Corresponding author.
E-mail address: alaa.ibrahim@uni.lu (A.A. Ibrahim).

https://doi.org/10.1016/j.csite.2026.107774
Received 26 September 2025; Received in revised form 26 December 2025; Accepted 29 January 2026

laboratory-scale module across a broad range of operating conditions, including feed temperatures of 45–75 °C, flow rates of 11–33 kg/h, and salinity concentrations reaching 70 ppt. Results demonstrate that the Spiral spacer configuration achieved the greatest improvements, delivering up to 95 % higher permeate flux, more than 35 % lower in specific energy consumption, and up to 85 % higher in thermal efficiency relative to baseline spacer-free operation.

1. Introduction

Water and energy supply are inseparably linked, and both are under increasing pressure due to growing demand and climate change [1]. Freshwater scarcity and energy shortages have emerged as two of the greatest obstacles to sustainable development in many countries. Today, nearly half of global freshwater withdrawals are consumed in power generation, while seawater desalination is still heavily dependent on electricity [2].

Desalination of seawater and brackish water has therefore become a vital strategy to address freshwater scarcity. Over the past decades, a range of technologies has been developed, with some reaching commercial maturity and others remaining under investigation. These technologies can be broadly classified into membrane-based and thermal-based processes. Reverse osmosis (RO), a pressure-driven process, dominates the membrane category, while multi-stage flash (MSF) and multi-effect distillation (MED) remain the most widely applied thermal processes [3]. At present, RO accounts for approximately 84 % of the total desalination plants and contributes nearly 69 % of the global desalinated water supply. MSF and MED together account for about 25 %, while emerging techniques such as nanofiltration, electrodialysis, and others represent the remaining fraction [4]. Despite their success, these technolo-gies are constrained by key drawbacks.

RO requires transmembrane pressures exceeding 60 bar to treat seawater with ~3.5 % salinity, demanding significant pumping power. MSF and MED, on the other hand, require high-temperature operation, substantial thermal and electrical energy inputs, and encounter scaling and fouling challenges [5,6].

Although conventional large-scale desalination techniques like RO and thermal distillation processes (MSF and MED) are extensively utilized globally, their high energy demands and significant costs present challenges for smaller-scale and remote installations. This has driven growing attention toward low-temperature and renewable-energy-driven desalination technologies. These include humidification–dehumidification (HDH) systems and solar stills [7,8], which operate based on phase-change mechanisms and are particularly suited for distributed or standalone water generation systems. While such technologies offer simplicity and compatibility with solar energy, they generally suffer from low water productivity, large footprint, and limited scalability. Nevertheless, their development underscores the expanding research focus on thermal desalination methods that can process high-salinity brines while minimizing reliance on high-pressure systems and maximizing utilization of waste heat or sustainable thermal energy sources. Among these emerging thermal desalination technologies, Membrane Distillation (MD) has gained prominence as a promising next-generation solution.

MD technology thermally-driven separation through hydrophobic membrane technology to produce high-quality potable water while meeting stringent environmental regulations [6]. Unlike RO, where separation is governed by high hydraulic pressure, MD is driven by the difference in water vapor partial pressure across the membrane, which causes evaporation at the feed side of the membrane and condensation at the distillate side. Since its introduction more than four decades ago, MD has been recognized as a promising desalination technology due to its ability to operate at moderate temperatures (<80 °C), tolerate highly saline feeds, and utilize low-grade or renewable heat sources while maintaining a 100 % theoretical rejection of non-volatile solutes, and high recovery rate [9]. Based on condensation methods, MD can be implemented in four main configurations: direct contact (DCMD), vacuum (VMD), sweeping gas (SGMD), and air gap membrane distillation (AGMD) [10]. Compared with conventional desalination technologies such as multi-stage flash (MSF), multi-effect distillation (MED), and RO, MD offers several advantages, including high separation efficiency of non-volatile solutes (up to 30 times higher purity than RO); operation at much lower pressures (around atmospheric pressure or below) than RO (operating up to 80 bar [11]), reduced sensitivity to salinity, no extensive pretreatment, compact design, and the potential for direct integration with renewable energy sources, particularly solar heat [10–13]. These characteristics make MD an attractive and competitive alternative for sustainable desalination. Moreover, recent studies have demonstrated that MD permeate can achieve the high purity levels required for water electrolysis, making it suitable for direct green hydrogen production, particularly when combined with waste-heat recovery or other renewable heat sources [14–19]. Ultrapure water (UPW) with conductivities below 0.8 μS/cm has been successfully produced from drinking water using MD test setups [15]. Additionally, investigations have indicated that MD systems can generate distillate using the excess heat from electrolyzers at lower costs than conventional RO [16], demonstrating the potential of MD water as a reliable feed for hydrogen production while reducing pretreatment requirements [14]. Nevertheless, conventional MD modules are limited by significant heat losses associated with external feed heating, as well as temperature polarization (TP) the difference between bulk feed temperature and the membrane interface caused by latent heat of evaporation and conduction through the membrane. TP reduces the vapor pressure gradient across the membrane, thereby lowering permeate flux and increasing specific energy consumption [20].

Feed channel spacers have been introduced as an effective strategy for mitigating fundamental challenges in MD, including concentration and temperature polarization, limited flux, and membrane fouling. In addition to providing mechanical support to the membrane surface, spacers enhance hydrodynamic conditions within the flow channel by inducing turbulence, thereby improving mass transfer and mitigating polarization phenomena [21]. Since 2010, research on spacer design has expanded significantly, with novel geometries and materials increasingly explored to optimize performance and reduce energy consumption in membrane processes [22–27]. The present study experimentally investigates two innovative spacer designs (mixer and spiral) across three distinct geometric arrangements, with each design drawing inspiration from established mixing industry principles. These novel spacer geometries were initially introduced for membrane distillation applications through our previous numerical investigations [27], in which their performance was compared with a commercial spacer (denoted as Cy45°) and a another cylindrical filament-based spacer (denoted as Cy90°). The results demonstrated substantial performance enhancements, including an average improvement of approximately 88 % in mixing behavior and nearly doubling the Nusselt number for heat transfer, while maintaining minimal pressure drop penalties compared to empty channel configurations [27]. Building upon these promising numerical findings, this experimental investigation seeks to translate the computational performance gains into tangible operational benefits, specifically evaluating permeate flux production, specific energy consumption (kWh/m^3), and thermal efficiency performance within an air gap membrane distillation (AGMD) system. This work aims to demonstrate the practical viability of these innovative spacer designs for enhancing AGMD system performance and advancing sustainable desalination technology.

2. Materials and methods

2.1. AGMD system setup

The experimental setup comprised a laboratory-scale flat-sheet Air Gap Membrane Distillation (AGMD) module featuring two countercurrent fluid loops: a hot loop, through which the heated working fluid circulates, and a cold loop, through which the cooling water circulates. Within the hot loop, a heating circulator equipped with an external coiled bath tank was employed to heat the working fluids, which were controlled by different flow rates before entering the feed channel (entrance diameter of 6 mm). In the cold loop, a cooling circulator was used to maintain the temperature of the water in the cold channel. Both the feed and cold channels were identical in length, width, and height, measuring 254 mm × 10 mm × 4 mm, respectively, while the air gap had a height of 5 mm and shared the same length and width. Thermocouples were utilized to measure the inlet and outlet temperatures in both loops, while a pressure sensor monitored the inlet pressure to the feed channel. Fresh permeate was collected and weighed using a sensitive precision balance, and an electrical conductivity meter was employed to assess the electrical conductivity of the four different feedwater and permeate. Details of the devices used in this setup are listed in Table 1. The AGMD module was equipped with a hydrophobic membrane crafted from microporous polyethylene, utilizing ultra high molecular weight polyethylene (UHMW-PE). The specifications for this membrane are detailed in Table 2.

2.2. Experimental procedure and operating conditions

Prior to each experimental procedure, the AGMD laboratory module underwent a thorough inspection for leaks and was cleaned to ensure consistent performance. Since the module is made of stainless steel, special attention was given to sealing. To prevent any vapor escape through gaps, the module was carefully sealed using customized silicone flat gaskets, ensuring reliable tightness throughout the experiments. The feed water was prepared to simulate three distinct types of saline water: brackish water, ocean/sea water, and hypersaline water. These solutions were formulated by dissolving 100 % natural, additive-free salt sourced from the Guérande Sea (France) into tap water characterized by very low baseline salinity. The salinity levels for each simulated water type are detailed in Table 3. The prepared feed solution was introduced into the hot loop reservoir, and the system was subsequently assembled and primed. The heating and cooling circulators were activated to achieve the desired inlet temperatures, and the system was allowed to reach steady-state conditions.

To assess the performance of the AGMD system using four types of feedwater (tap water plus the three saline water types), two sets of experiments were conducted: one set under a constant feed temperature of 65 °C with varying flow rates, and another set under a constant flow rate of 27 kg/h with varying feed temperatures. The complete set of operating conditions for all experiments is summarized in Table 4.

The flow regime within the feed channel was characterized by calculating the Reynolds number for all flow rates investigated. Based on the channel geometry and operating conditions, the Reynolds numbers corresponding to feed flow rates of 15, 21, 27, and 33 kg/h were approximately 1270, 1780, 2280, and 2790, respectively. These values indicate that the flow remained laminar at the lower flow rates and approached the laminar–transitional boundary at the highest flow rate. When the spacer was inserted, localized

Table 1
Devices used for system operation and data collection.

Device name	Model	Key specification
Heating Circulator	SL-6, JULABO USA, Inc.	Temperature stability ±0.01 °C
Refrigerated Circulator	F32-ME, JULABO USA, Inc.	Temperature stability ±0.01 °C
Thermocouples (TC)	Type T Class 1, OMEGA.CO.UK.	Accuracy: ±0.5 °C
Pressure Sensor	PXM309-002G10V, OMEGA.CO.UK.	Accuracy: ±0.25 % FS[a]
Conductivity portable meter	HQ430D, HACH, USA.	Resolution: 0.01 μS/cm - 0.1 mS/cm
Precision Balance	JET4002G, METTLER TOLEDO, USA.	Resolution: 1d[b] = 0.01 g

[a] FS represents the full-scale range and includes linearity, hysteresis, and repeatability, calculated using the Best Straight Line (BSL) method.

[b] Refers to a one-scale division, which is the smallest increment the balance can display.

Table 2
Membrane specifications.

Properties	Value
Material	Polyethylene (PE)
Membrane thickness	110 μm
Membrane Porosity	0.85
Membrane pore size	0.20 μm
Air permeability, Gurley number	12.5 s/50 mL
Tensile strength (machine direction)	25 Mpa
Tensile strength (transverse direction)	21 Mpa
Membrane total area	2.54×10^{-3} m^2

Table 3
Feedwater properties.

Name	Simulated Water type	Salinity (S) [ppt][c]	Electrical Conductivity[d] (σ) [μS/cm]
S1	Tap water	0.23	383
S2	Brackish water	15	25300
S3	Ocean/Sea water	36	60200
S4	Hypersaline	70	118000

[c] Parts per thousand (ppt).
[d] The electrical conductivity values were measured at an ambient temperature of 19 °C.

Table 4
Operating conditions.

Parameter	Value
Inlet feed temperature (T_h) [°C]	45, 55, 65, and 75
Feed flow rate (Q) [kg/hr]	15, 21, 27, and 33
Inlet cold temperature (T_c) [°C]	14.5

turbulent flow patterns developed around the spacer filaments, generating additional mixing and disrupting the boundary layer. Therefore, any improvement in heat and mass transfer is primarily attributed to these spacer-induced local hydrodynamic effects rather than to fully developed turbulent flow.

$$Re = \frac{\rho v D_h}{\mu} \tag{1}$$

where ρ [kg/m^3] and μ [Pa·s] are the fluid density and dynamic viscosity, v is the bulk velocity, and D_h is the hydraulic diameter of the channel. The fluid properties were evaluated at a representative bulk operating temperature of 60 °C, corresponding to the midpoint of the experimental temperature range.

2.3. Spacer-filled AGMD

Three spacers' configurations (Fig. 2) were implemented in the feed channel to investigate their impact on AGMD performance: a single-filament mixer spacer (Mix-1), a three-filament mixer spacer (Mix-2), and a single-filament spiral spacer (Spiral), each compared against a baseline empty channel (No-spacer) configuration. Previously we reported three-filament mixer and spiral spacer designs, which demonstrated enhanced mixing and heat transfer characteristics in our prior numerical analysis [27] A newly developed single-filament mixer spacer was incorporated to investigate the influence of active membrane surface area, void fraction, and overall system performance. The characteristics of all studied configurations are summarized in Table 5.

The mixer spacer, which replicates a twisted tape/Kenics-type structure, were designed with intersecting filaments to promote turbulence and enhance both heat and mass transfer within the feed channel. The spiral spacer, resembling the low-pressure drop (LPD) type, featured a helical geometry aimed at inducing swirling flow, thereby reducing temperature polarization along the

Table 5
Geometrical characteristics of feed channel Configurations.

Spacer name	Void fraction (Ɛ)	Contact area [m^2]	Membrane active area (A_M%)
No-spacer	1	0	100 %
Mix-1	0.9568	121.019	95.4 %
Mix-2	0.8704	363.057	85.71 %
Spiral	0.9194	241.205	90.50 %

membrane surface. Both spacers were fabricated using a SLA printer, brand Prusa, Model SL1S and manufactured using Prusament Model Resin (Prusa Research, Prague, Czech Republic). Each spacer was designed to match the feed channel's height (4 mm) and length (254 mm), ensuring a proper fit and maintaining consistent flow geometry. Following the experiments, the spacers were examined, and no deformation, swelling, cracking, or surface softening was observed. A post-use photograph (Fig. 1S) of the spacer is provided in the supplementary data file. All spacers were placed in direct contact with the membrane surface within the feed channel. The no-spacer configuration served as a control to establish baseline AGMD performance in the absence of any flow-altering structures.

2.4. *Performance parameters*

2.4.1. *Permeate flux (J)*

During the experiments, a temperature gradient was maintained between the hot and cold channels to establish a vapor pressure difference, which acts as the primary driving force for water vapor generation in the feed channel. The hydrophobic nature of the membrane prevents liquid water from passing through, permitting only vapor to cross the membrane. Upon reaching the air gap and encountering the cooled condensing surface on the opposite side, the vapor undergoes condensation, resulting in the formation of the permeate flux which represents the freshwater output from the device.

The permeate flux, denoted as J [kg/m^2 h], was determined using the gravimetric method (Eqn. (2)) [28]. In this context, m represents the accumulated mass of permeate [kg] that traversed the total effective membrane area A [m^2] over the entire distillation period t [h].

$$J = \frac{m}{A\ .\ t} \tag{2}$$

2.4.2. *Specific energy consumption (SEC)*

The specific energy consumption (SEC) is defined as the total energy input required to produce one cubic meter of distillate, expressed in (kWh/m^3). It comprises two primary components: the specific thermal energy consumption (STEC), which is highly dependent on the feedwater temperatures and reflects the thermal energy demand per unit volume of freshwater produced; and the specific electrical energy consumption (SEEC), which, in the context of this study, corresponds to the electrical energy consumed by the circulation pump during the distillation process [29]. The total SEC is given by:

$$SEC = STEC + SEEC \tag{3}$$

The STEC is calculated as:

$$STEC = \frac{Q_t\ .\ \rho}{J.\ A} \tag{4}$$

Where ρ is the density [kg/m^3], and Q_t is the total heat energy in [kW] and can be calculated using this equation:

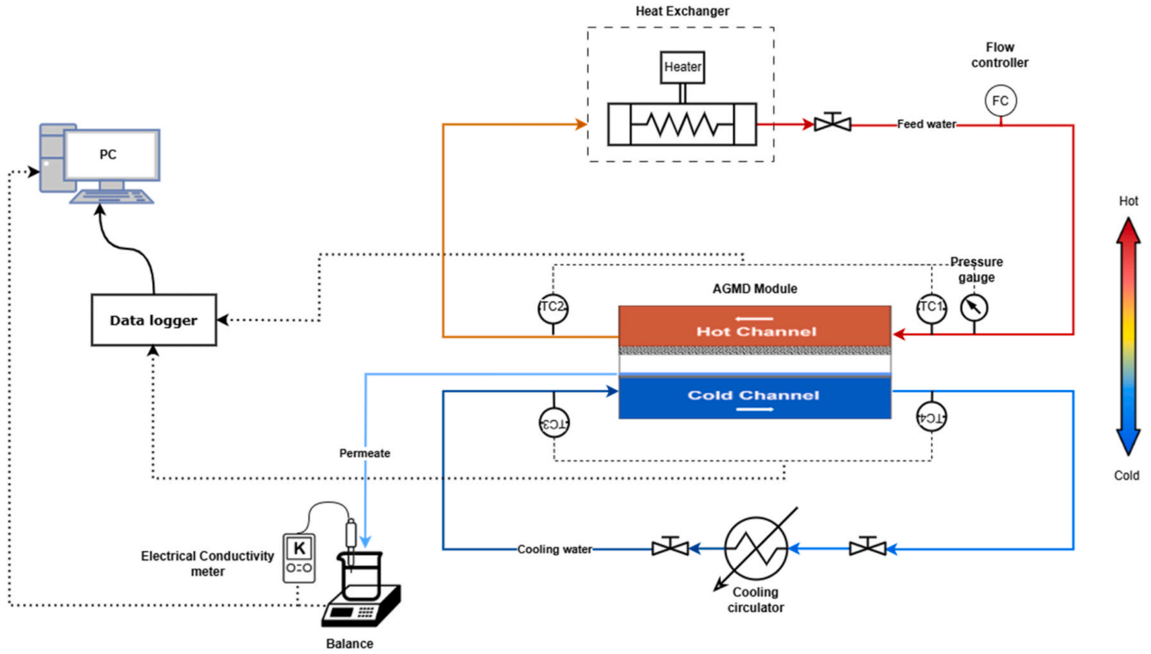

Fig. 1. Schematic diagram for the test facility.

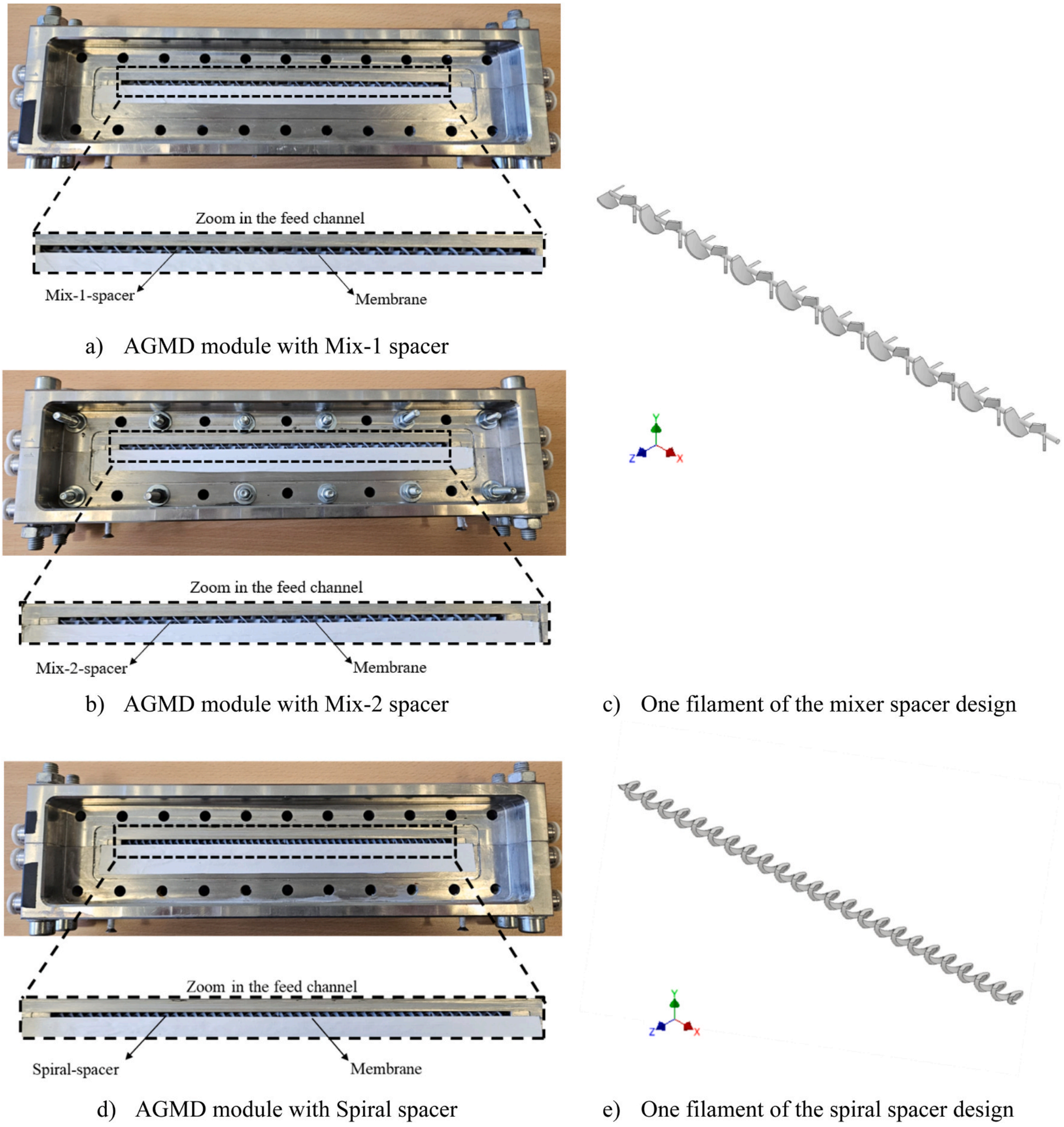

a) AGMD module with Mix-1 spacer

b) AGMD module with Mix-2 spacer

c) One filament of the mixer spacer design

d) AGMD module with Spiral spacer

e) One filament of the spiral spacer design

Fig. 2. AGMD module with two spacers' configurations: a) with Mix-1 spacer, b) with Mix-2 spacer, c) mixer spacer design, d) with spiral spacer, and e) spiral spacer design (Additional close-up images are provided in Figs. 2S and 3S).

$$Q_t = \dot{m}_f \,.\, C_p \,(T_{h.in} - T_{h.out}) \tag{5}$$

Where $\dot{m}_f$ is the mass flow rate of the feedwater [kg/s], C_p is the feed specific heat capacity (kJ/kg.°C), and $T_{h.in}$ and $T_{h.out}$ are the inlet and outlet temperatures of the feedwater, respectively.

While the STEC is calculated as:

$$SEEC = \frac{\dot{W}_{cir} \cdot \rho}{J.A} \tag{6}$$

Where $\dot{W}_{cir}$ is the electrical energy consumption of the feed flow pump in [KW] and can be calculated using this equation:

$$\dot{W}_{cir} = \frac{\dot{m}_f \,.\, \Delta P}{1000 \,.\, \rho \,.\, \eta_{pump}} \tag{7}$$

Where ΔP [Pa] denotes the pressure difference across the feed stream, measured between the inlet and outlet, and η_{pump} is the mechanical efficiency of the feed pump, assumed to be 0.8.

2.4.3. Thermal efficiency (TE)

The thermal efficiency (TE) in MD quantifies the fraction of supplied thermal energy that is effectively utilized for water phase change. This parameter represents the ratio between the latent heat consumed during vapor generation and the total heat input delivered to the feed solution throughout the distillation operation. It can be expressed as [30]:

$$TE\% = \frac{J.A.\Delta H_v}{\dot{m}_f.C_p.(T_{h.in} - T_{h.out})} \times 100 \tag{8}$$

Where ΔH_v is the latent heat of vaporization (KJ/kg).

2.4.4. Salt rejection (SR)

Salt rejection (SR) quantifies the MD system's capacity to retain non-volatile solutes, predominantly salts, thereby preventing their transport to the permeate stream. In the present study, electrical conductivity (σ) served as a proxy measurement for total dissolved solids (TDS) concentrations in both feed and permeate solutions. AGMD provides a significant advantage through its ability to maintain consistently high salt rejection rates [31]. Accordingly, SR was calculated as:

$$SR\% = \left(1 - \frac{\sigma_p}{\sigma_f}\right) \times 100 \tag{9}$$

Where σ_p and σ_f are the feed and permeate electrical conductivity in [μS/cm], respectively.

3. Results and discussion

Four AGMD configurations were subjected to systematic performance evaluation under varied operational conditions. The experimental program encompassed four salinity concentrations (0.2–70 ppt), four feed temperatures (45–75 °C), and four flowrate conditions (15–33 kg/h), generating a dataset of 128 experiments. This extensive experimental framework facilitated detailed characterization of AGMD performance across a wide range of operational parameters. The spacer configurations examined in this study were specifically designed to enhance internal flow dynamics, promote mixing characteristics, and minimize temperature polarization phenomena. This section presents an analysis of how spacer architecture and feed solution salinity collectively influence critical performance metrics, including permeate flux, thermal efficiency, and specific energy consumption.

Each experiment was performed for approximately 120 min. The system was allowed to thermally stabilize for 50–60 min prior to data collection. Steady state was defined as a temperature fluctuation $\leq \pm 0.5$ °C at all temperature measurement points. Data for flux and conductivity were recorded after stabilization for the remainder of the experiment. Under these conditions, no significant flux drift was observed once steady state had been achieved, and no membrane wetting was detected. Fouling was, however, observed for the hypersaline feed (70 ppt).

3.1. Effect of salinity on permeate flux across AGMD configurations

Fig. 3 illustrates the effect of salinity on permeate flux in the no-spacer AGMD configuration, which serves as the baseline configuration in this study, under two operating conditions. At a constant inlet temperature of 65 °C (Fig. 3a), the permeate flux increased with increasing feed flow rate due to enhanced turbulence and the corresponding reduction in temperature polarization at the membrane surface. For the lowest salinity (0.2 ppt, representing tap water), flux increased by 40 % as the flow rate increased from

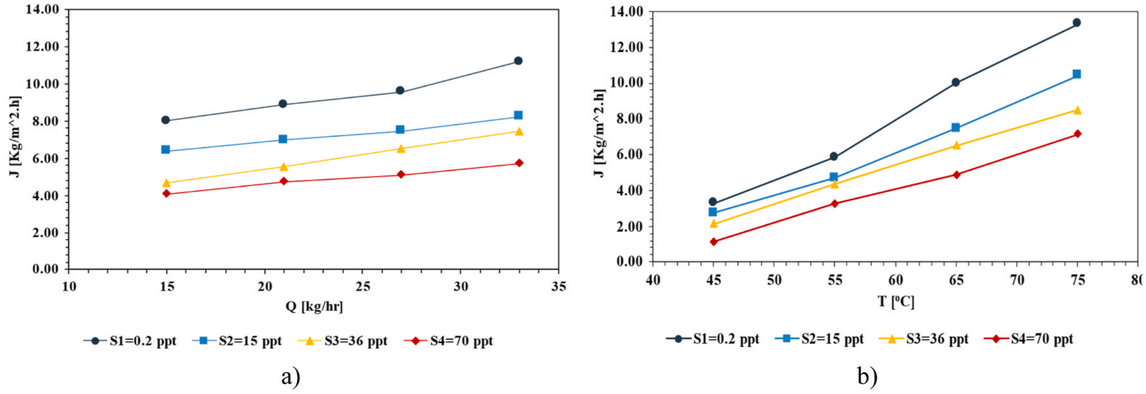

Fig. 3. Effect of salinity on permeate flux (J) in the no-spacer AGMD configuration: a) at constant inlet feed temperature of 65 °C, and b) at constant inlet feed flow rate of 27 kg/h.

10 to 35 kg/h. For brackish water conditions (15 ppt), the increase was around 29 %, whereas for seawater salinity (36 ppt), flux increased by nearly 60 %. At the highest salinity tested (70 ppt, representing brine), the increase was about 40 %. Although the flux improved with feed flow rate, its absolute magnitude decreased with salinity because of the reduced vapor pressure associated with higher salt concentrations.

At a constant feed flow rate of 27 kg/h (Fig. 3b), permeate flux exhibited a pronounced dependence on feed temperature. As the inlet temperature increased, the vapor pressure gradient across the membrane was amplified, resulting in a substantial enhancement in flux. For tap water (0.2 ppt), brackish water (15 ppt), and seawater (36 ppt), the flux increased by about 300 % as the inlet temperature rose from 45 to 75 °C. At the highest salinity (70 ppt, representing brine), the flux increased by nearly 530 % over the same temperature range. However, the negative impact of salinity was again evident, with reduced flux at higher salt concentrations.

It is important to note that at 70 ppt, in addition to the reduction in flux caused by decreased vapor pressure, fouling effects were visually detected (Fig. 1S). This indicates that highly concentrated brines not only suppress vapor transport thermodynamically but also introduce operational challenges related to salt deposition, which may lead to long-term flux decline.

Overall, these results confirm that while both temperature and flow rate positively influence permeate flux, salinity consistently suppresses performance, with feed temperature emerging as the most dominant factor.

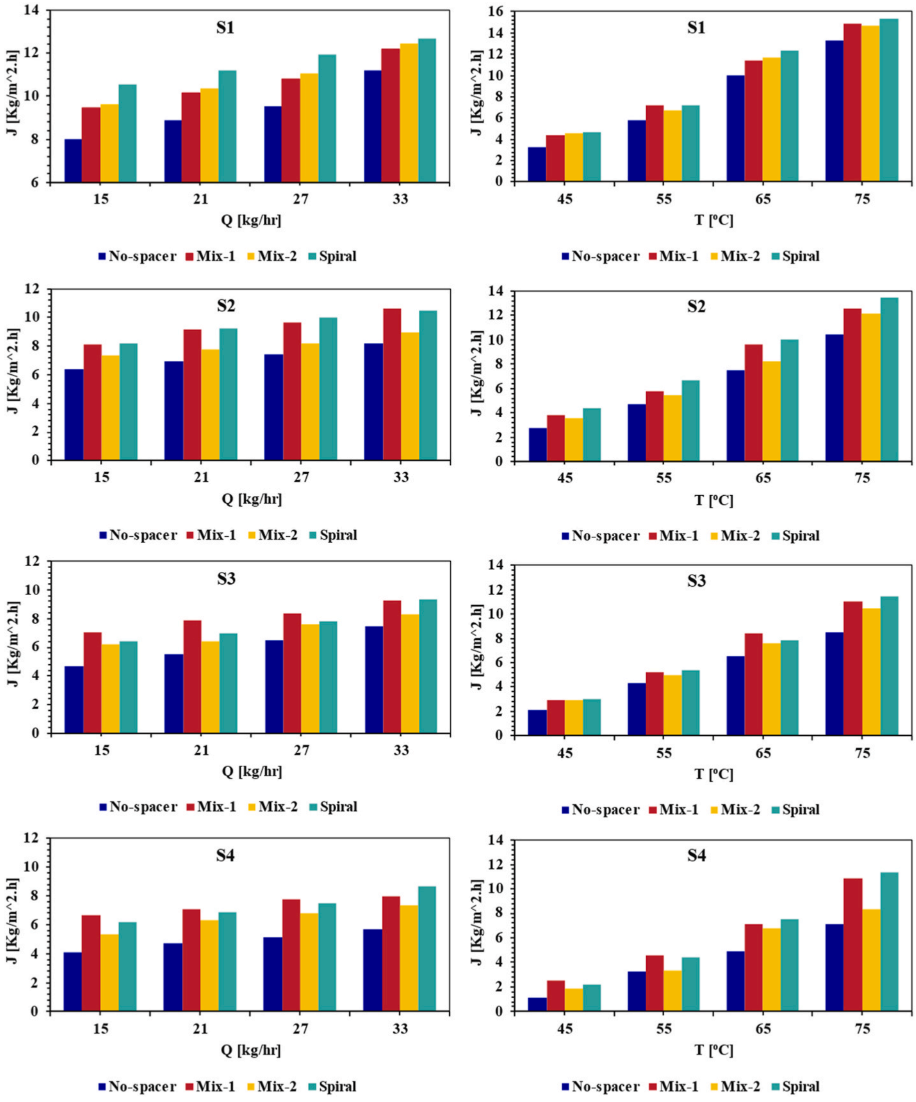

Fig. 4. Variation of Permeate flux (J) with feed flow rate (Q) at constant T of 65 °C, and feed temperature (T) at constant Q of 27 kg/h for different spacer configurations (No-spacer, Mix-1, Mix-2, and Spiral) across modules S1–S4.

3.2. *Influence of spacer design on permeate flux*

Fig. 4 presents the variation of permeate flux across four AGMD configurations (No-spacer, Mix-1, Mix-2, and Spiral) at different salinity levels (S1–S4). The corresponding absolute flux values are provided in Table 1S in the supplementary information. In all cases, the use of spacers enhanced the flux compared to the baseline no-spacer channel, confirming their beneficial role in improving hydrodynamics and heat transfer within the AGMD module. At low salinity (S1), the Spiral configuration provided the highest enhancement, with permeate flux about 32 % higher than the no-spacer design at the maximum feed flow rate (33 kg/h), and up to 41 % higher at the highest tested temperature (75 °C), followed by Mix-2 and Mix-1. As salinity increased (S2 to S4), corresponding to cases where salt was added to the feed water, the Spiral spacer continued to provide the greatest enhancement, producing fluxes approximately 28 %, 38 %, and 52 % higher than the no-spacer configuration at the maximum feed flow rate (33 kg/h), and about 59 %, 43 %, and 95 % higher at the highest tested temperature (75 °C), respectively. Under these conditions, the performance ranking shifted, with Mix-1 generally outperforming Mix-2, while both remained below the Spiral design.

This shift can be explained by differences in active membrane area, as shown in Fig. 5: although Mix-1 and Mix-2 share the same filament design, Mix-1 exposes a larger fraction of the membrane surface ($A_M\,\% = 95.4$) compared to Mix-2 ($A_M\,\% = 85.7$). Although Mix-2 promotes stronger turbulence at low salinity, its higher degree of surface coverage reduces the effective membrane area available for vapor transport, which becomes particularly detrimental as salinity increases and the vapor pressure driving force is already diminished. In contrast, the larger active area in Mix-1 allows more effective utilization of the membrane surface, giving it a performance advantage over Mix-2 under saline conditions. This highlights a fundamental design trade-off: while both spacers provide mixing benefits, maximizing the active area is more critical for sustaining flux at higher salinities. Overall, the results confirm that spacer integration is effective in mitigating polarization effects and enhancing flux, with the Spiral geometry consistently providing the greatest improvement, and Mix-1 performing more robustly than Mix-2 under saline conditions due to its higher exposed active area.

Across all studied cases, the permeate quality demonstrated the strong salt rejection capability of the AGMD module. Fig. 6 illustrates the variation of average salt rejection (SR%) with feed salinity. SR% measured across all tested operating conditions are provided in Table 4S in supplementary information. For all salted feedwater > conditions (S2–S4: brackish, seawater, and brine), corresponding to salinities between 25,300 and 118,000 ppt, the membranes maintained excellent rejection, with SR% consistently above 99.3 %. Only minor variations were observed across the tested conditions, and no significant decline in performance was detected even at the highest salinity levels. These results confirm the robustness of the AGMD process in maintaining stable separation efficiency and ensuring high-quality permeate under increasingly saline feedwater conditions.

3.3. *Influence of spacer design on pressure drop (ΔP)*

Fig. 7 illustrates the effect of spacer geometry on the feed-channel pressure drop (ΔP) as a function of feed flow rate in the AGMD module. For all configurations, ΔP increases monotonically with increasing flow rate, reflecting the expected rise in hydraulic

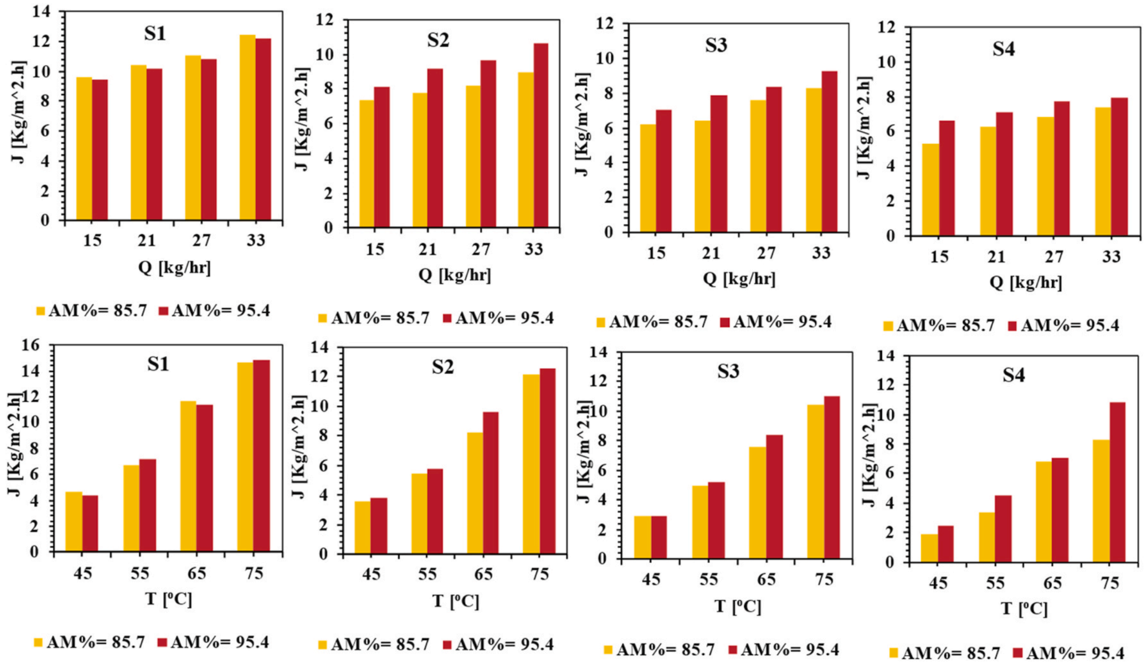

Fig. 5. Effect of active membrane area (AM%) on permeate flux under different salinity > conditions (S1–S4) as a function of feed flow rate (Q, top row) at constant T of 65 °C, and feed temperature (T, bottom row) at constant Q of 27 kg/h.

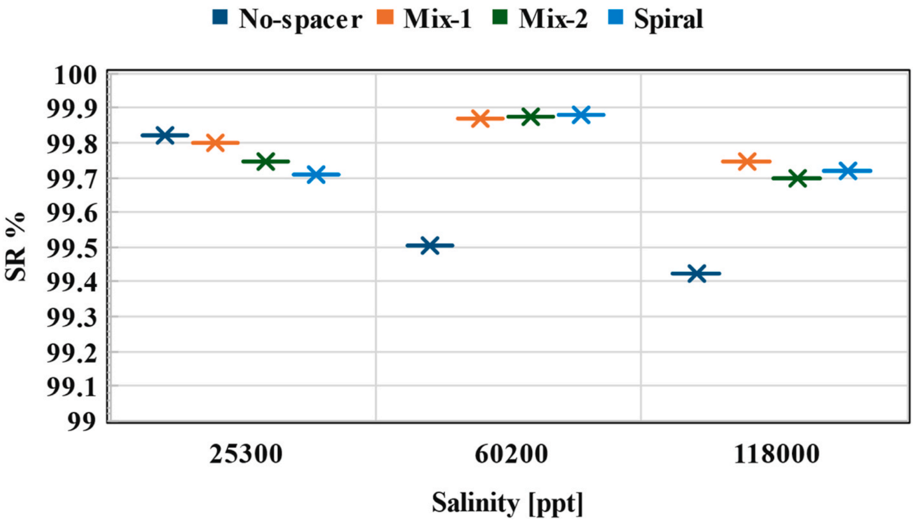

Fig. 6. Variation of average salt rejection (SR%) with feed salinity for four AGMD configurations.

resistance with higher axial velocities. Spacer-filled channels exhibit higher pressure losses than the empty channel due to increased flow obstruction and enhanced hydrodynamic interactions induced by the spacer structures. The empty channel consistently shows the lowest pressure drop, with ΔP values ranging from approximately 400 to 3500 Pa over the investigated flow rates. Among the spacer configurations, the Mix-2 spacer produces the highest pressure drop across all examined flow rates, which can be attributed to the presence of three mixer filaments that significantly increase flow resistance. In contrast, the Mix-1 and Spiral spacers exhibit comparable pressure-drop values, indicating similar hydraulic behavior despite differences in their geometrical design.

Fig. 8 presents the corresponding permeate flux for each configuration under the same operating conditions. As expected, the permeate flux increases with increasing feed flow rate for all cases, which is associated with enhanced convective heat transfer, reduced thermal boundary-layer thickness, and mitigation of temperature polarization effects. Although higher feed flow rates and spacer-induced mixing led to increased pressure drop, the associated electrical energy demand remains relatively small. Since membrane distillation is predominantly governed by thermal energy input, the overall energy consumption is mainly dictated by thermal effects rather than pumping power [32,33]. Consequently, the observed increase in pressure drop does not offset the substantial gains in permeate flux achieved through tested spacer design.

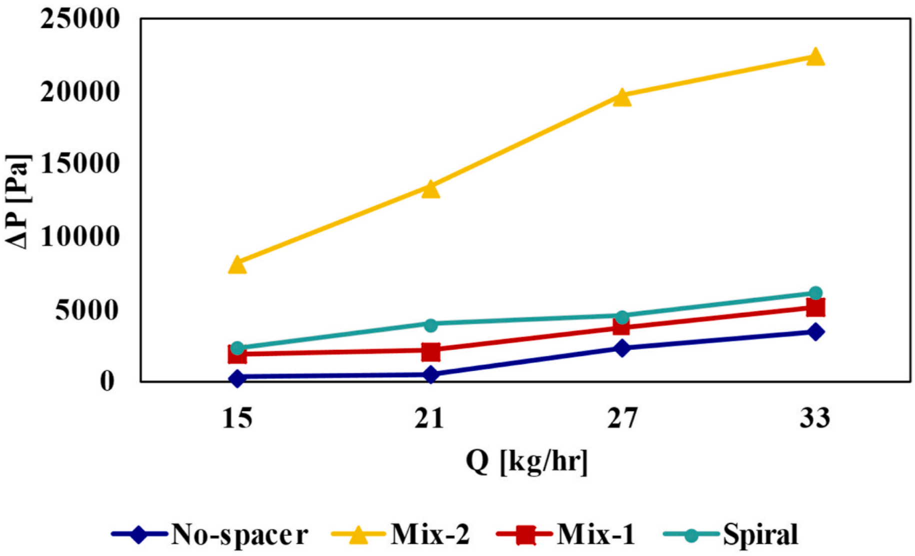

Fig. 7. Effect of spacer geometry on the feed-channel pressure drop (ΔP) as a function of feed flow rate in the AGMD module using simulated seawater (S3).

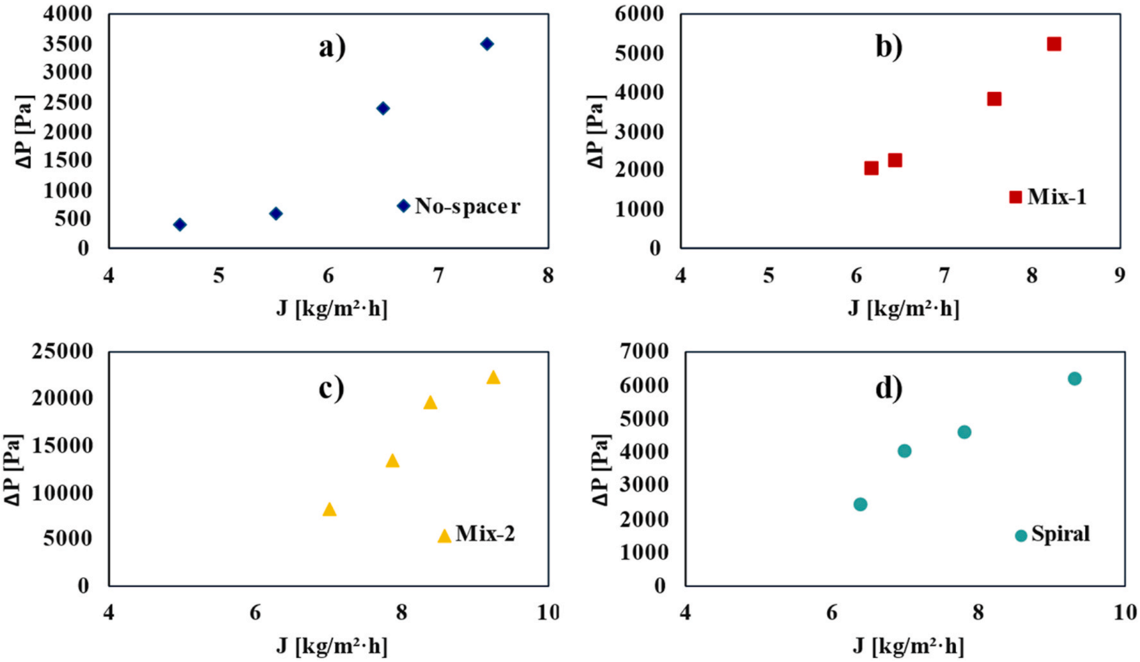

Fig. 8. Feed-channel pressure drop (ΔP) vs. permeate flux (J) for different AGMD configurations: a) empty channel (no spacer), b) Mix-1 spacer, c) Mix-2 spacer, and d) Spiral spacer. The data corresponds to the same operating conditions used in Fig. 7.

3.4. *Specific energy consumption (SEC) analysis*

The results demonstrate the effect of operating conditions and spacer configuration on the SEC in AGMD systems. As shown in Fig. 9, SEC exhibits an inverse relationship with feed flow rate across all tested configurations (S1–S4). The corresponding SEC values are provided in Table 2S in the Supplementary Information. In the absence of spacers, the laminar flow regime results in SEC reduction primarily through increased axial velocity, which slightly decreases the thermal boundary layer thickness, reduces the bulk feed temperature drop, and mitigates polarization effects. When spacers are introduced, however, the flow behavior is fundamentally modified by the promotion of flow disturbance and localized turbulence. These hydrodynamic effects significantly enhance mixing, minimize polarization phenomena, and improve both heat and mass transfer coefficients, ultimately yielding higher vapor transport efficiency, greater permeate flux, and reduced thermal losses.

A similar trend is observed with respect to feed temperature, where increasing the feed temperature leads to a reduction in SEC. This behavior is attributed to the sharp increase in vapor pressure difference across the membrane at elevated temperatures, which strengthens the thermodynamic driving force for vapor transport. Consequently, higher feed temperatures yield enhanced permeate flux while simultaneously reducing the energy requirement per unit volume of produced distillate.

The specific electrical energy consumption (SEEC), presented in Fig. 10, quantifies the pumping energy demand expressed in Wh/m^3. The Mix-1 and Spiral spacer configurations exhibit comparable SEEC values, whereas the Mix-2 spacer shows higher SEEC due to its increased pressure drop characteristics. Nevertheless, the SEEC values remain substantially lower than the specific thermal energy consumption (STEC), indicating that thermal energy requirements dominate the overall energy balance. Consequently, the total SEC is predominantly determined by thermal energy input, with electrical energy representing a negligible contribution.

The comparative assessment of spacer configurations highlights distinct performance characteristics. The no-spacer configuration consistently exhibits the highest SEC, reflecting limited heat and mass transfer performance. In contrast, the Spiral and Mix-1 spacer designs generally achieve the lowest SEC values, underscoring the benefits of optimized flow patterns and enhanced mixing. Overall, these findings confirm that both operating conditions, particularly high feed flow rate and temperature, and spacer geometry strongly influence AGMD performance, with advanced spacer designs offering substantial energy savings.

The SEC measured in the present experimental study is higher than some values reported in the literature [29,30,32]. This discrepancy can be primarily attributed to the design and construction of the AGMD module employed in this work, which was fabricated in-house using stainless steel components. While stainless steel provides structural robustness and chemical resistance, its relatively high thermal conductivity promotes increased heat losses to the surrounding environment, thereby increasing the overall thermal energy demand of the system. These additional heat losses are consequently reflected in elevated SEC values. To mitigate this effect, future AGMD module designs should consider the use of materials with lower thermal conductivity and/or enhanced thermal insulation, which could significantly reduce heat losses and improve the overall energetic efficiency of the process.

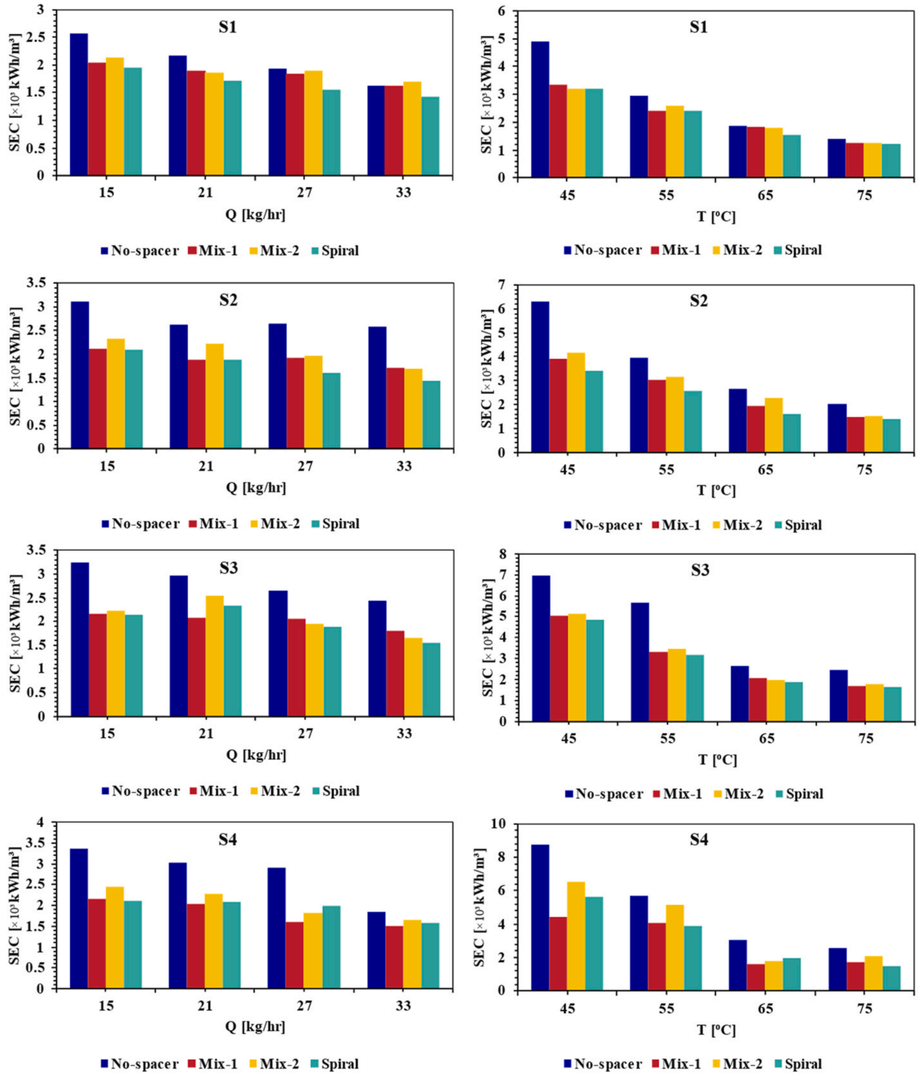

Fig. 9. Variation of Specific Energy Consumption (SEC) with feed flow rate (Q) at constant T of 65 °C, and feed temperature (T) at constant Q of 27 kg/h for different spacer configurations (No-spacer, Mix-1, Mix-2, and Spiral) across modules S1–S4.

3.5. *Thermal efficiency (TE) evaluation*

The thermal efficiency (TE%) data presented in Fig. 11 demonstrate positive correlations with both feed flow rate and feed temperature across all tested modules (S1–S4). The corresponding TE% values are provided in Table 3S in the Supplementary Information. This trend contrasts with the inverse relationship observed for SEC, reflecting the complementary nature of these two performance indicators. With increasing flow rate, TE% improves because higher velocities reduce the extent of temperature drop along the feed channel, allowing a larger fraction of the input heat to contribute to vapor generation. The influence of feed temperature is even stronger, as higher temperatures amplify the vapor pressure gradient across the membrane, thereby increasing vapor flux and improving the utilization of thermal energy.

The comparative analysis of spacer designs further reinforces this behavior. The no-spacer case consistently yields the lowest TE%, reflecting limited heat transfer and poor energy utilization. In contrast, the Spiral and Mix-2 spacers achieve the highest TE% values, confirming the benefits of optimized hydrodynamics and enhanced mixing in promoting more effective use of thermal input. Overall, the findings demonstrate that both feed flow rate and temperature, together with appropriate spacer geometry, play critical roles in maximizing the thermal efficiency of AGMD.

3.6. *Overall performance comparison*

Fig. 12 details the percentage changes in permeate flux (J), specific energy consumption (SEC), and thermal efficiency (TE%)

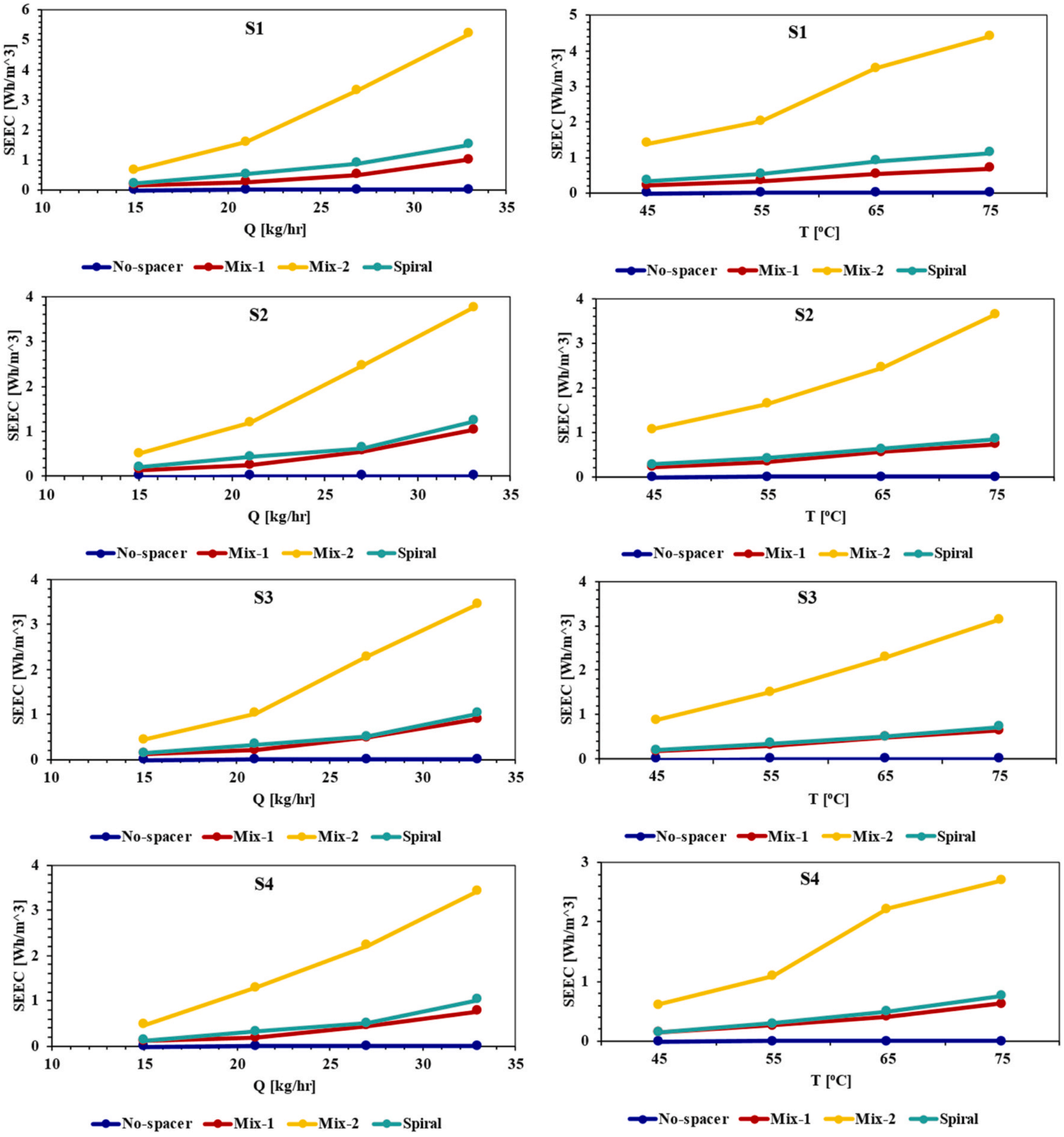

Fig. 10. Variation of Specific Electrical Energy Consumption (SEEC) with feed flow rate (Q) at constant T of 65 °C, and feed temperature (T) at constant Q of 27 kg/h for different spacer configurations (No-spacer, Mix-1, Mix-2, and Spiral) across modules S1–S4.

relative to the no-spacer case for each module and operating condition. The results clearly demonstrate the benefits of incorporating spacers into AGMD modules. Across all operating ranges, the use of spacers leads to substantial increases in permeate flux (J) and thermal efficiency (TE%), accompanied by notable reductions in specific energy consumption (SEC). Among the evaluated designs, the Spiral spacer generally provides the greatest improvements, with both flux and TE% increasing by 60–70 %, compared to about 50 % for Mix-1 and 20–40 % for Mix-2 at higher feed temperatures, while simultaneously lowering SEC by more than 30 % in several modules. The positive impact of spacers is particularly evident at elevated feed temperatures and higher flow rates, where stronger vapor pressure gradients amplify the effects of enhanced mixing and heat transfer. Overall, the findings confirm that the proposed spacer designs significantly improve AGMD performance by enabling higher distillate production with lower energy requirements and higher thermal efficiency.

3.7. Spacer geometry and performance

While analyzing the experimental data, we found that the spiral spacer design, which provides an effective membrane area

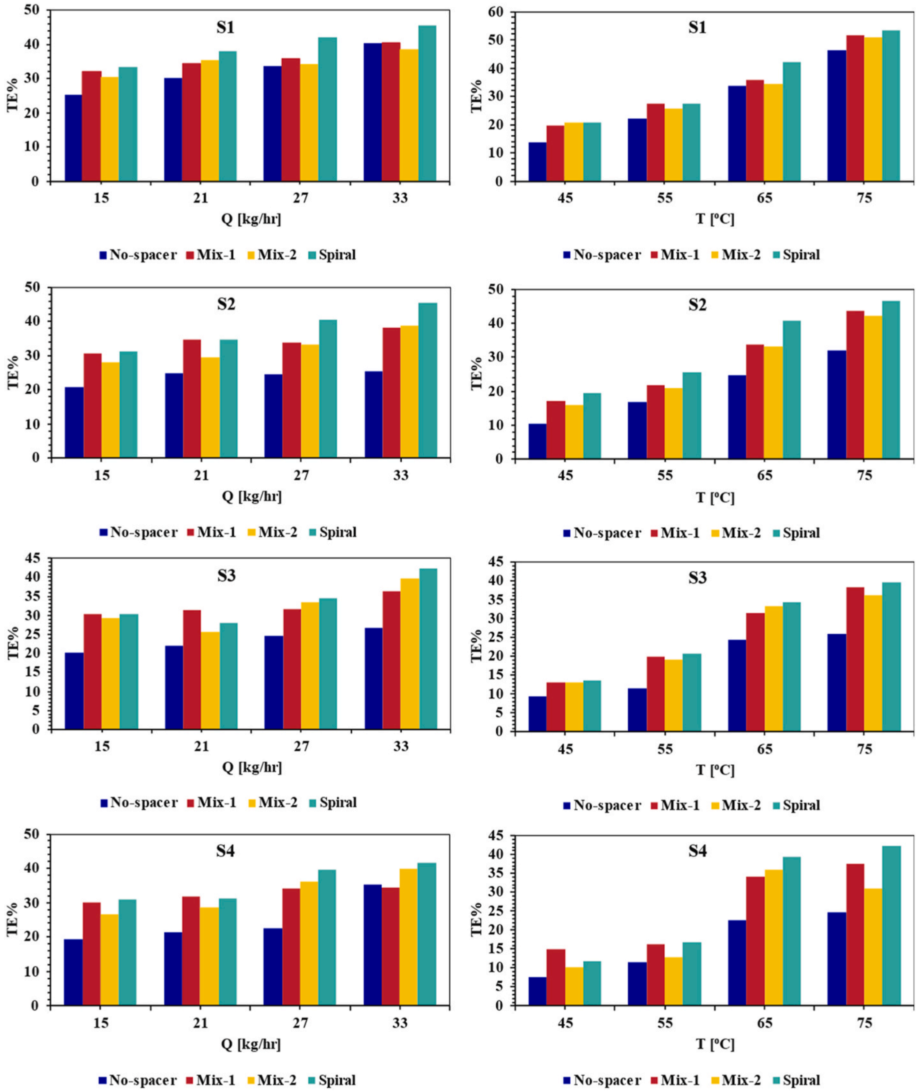

Fig. 11. Variation of Thermal efficiency (TE%) with feed flow rate (Q) at constant T of 65 °C, and feed temperature (T) at constant Q of 27 kg/h for different spacer configurations (No-spacer, Mix-1, Mix-2, and Spiral) across modules S1–S4.

utilization of about 90 %, delivers the best overall performance when operating with saline feed water. As shown in Fig. 13, the 90 % active membrane area associated with the Spiral spacer achieves the highest flux values across salinities S2–S4 at the highest tested temperature (75 °C) and feed flow rate (33 kg/h). This is followed by the performance of Mix-1 (AM% = 86), while the lowest flux is observed with Mix-2 (AM% = 95). These results indicate that membrane active area alone does not govern permeate flux, as spacer filament geometry and the hydrodynamics it induces also play critical roles in AGMD performance. However, when comparing spacers that share the same filament design, we found that a larger active membrane area consistently resulted in higher flux. Therefore, we can conclude that optimizing both the active membrane area and the spacer design is essential for maximizing permeate flux and overall AGMD performance.

4. Conclusion

This investigation presented and experimentally assessed three innovative spacer designs (Mix-1, Mix-2, and Spiral) within a laboratory-scale AGMD system across diverse operational parameters. The experimental findings revealed that permeate production rates are predominantly governed by feed temperature and flow rate, whereas elevated salinity levels diminish flux through reduced vapor pressure differentials. The incorporation of spacer elements substantially improved system performance by alleviating polarization effects and enhancing flow dynamics, with the Spiral design delivering the most significant performance improvements.

Relative to the no-spacer reference case, the Spiral spacer demonstrated remarkable, including flux increases of up to 95 % under hypersaline feed conditions (70 ppt) at 45 °C and a flow rate of 27 kg/h, specific energy consumption reductions exceeding 30 % across

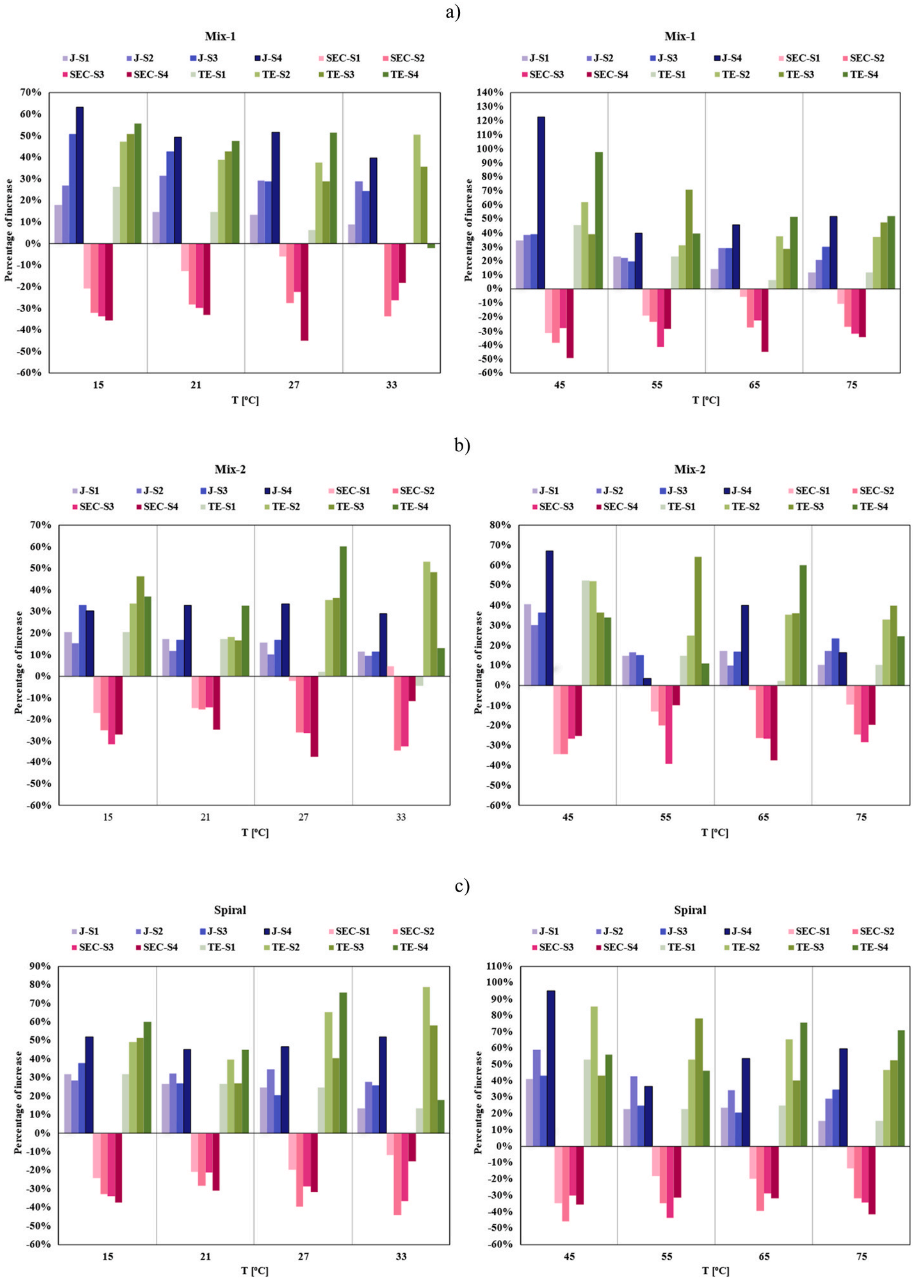

Fig. 12. Percentage change in permeate flux (J), specific energy consumption (SEC), and thermal efficiency (TE%) relative to the no-spacer configuration, as a function of feed flow rate (Q) at constant T of 65 °C, and feed temperature (T) at constant Q of 27 kg/h for different spacer designs: a) Mix-1, b) Mix-2, and c) Spiral, across modules S1–S4.

most tested conditions, and thermal efficiency improvements of up to 85 % under brackish feed conditions (15 ppt) at 45 °C and 27 kg/h. The Mix-1 configuration demonstrated greater performance stability at elevated salinities due to its higher effective membrane exposure, while Mix-2 highlighted the trade-off between enhanced turbulence and reduced active membrane area. All evaluated configurations sustained exceptional salt rejection capabilities of 99.8 % in most tests, even at salinities reaching 70 ppt, validating AGMD's reliability for high-concentration brine treatment applications.

The findings establish that advanced spacer geometries substantially improve AGMD operational performance, showing that flux is not governed by active membrane area alone but also by spacer filament geometry and the hydrodynamics it induces. This underscores the importance of simultaneously optimizing membrane exposure and spacer architecture to maximize system efficiency, with the Spiral configuration serving as a clear demonstration of this principle through its superior energy efficiency, thermal utilization, and water production capacity for desalination applications.

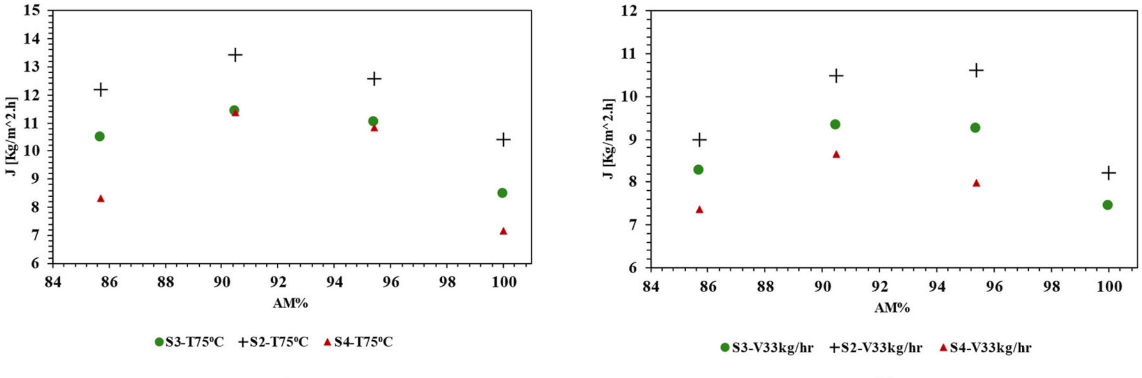

a) b)

Fig. 13. Effect of active membrane area (AM%) on permeate flux (J) at 75 °C and 33 kg/h.

CRediT authorship contribution statement

Alaa Adel Ibrahim: Writing – original draft, Validation, Methodology, Investigation, Data curation, Conceptualization. **Iurii Dolganov:** Writing – review & editing, Methodology. **Stephan Leyer:** Writing – review & editing, Supervision, Investigation.

Declaration of competing interest

The authors declare the following financial interests/personal relationships which may be considered as potential competing interests: Alaa Adel Ibrahim reports financial support was provided by FNR - Luxembourg National Research Fund. If there are other authors, they declare that they have no known competing financial interests or personal relationships that could have appeared to influence the work reported in this paper.

Acknowledgement

The presented findings are part of the EXPCOAGMD project (AFR-17022904) supported by the Fonds National de la Recherche (FNR), Luxembourg. The authors also acknowledge Mr. Bart Nelemans, Managing Director of Aquastill.nl, for providing the membranes used in this study and for facilitating a site visit, which contributed to the successful execution of the experiments.

Appendix A. Supplementary data

Supplementary data to this article can be found online at https://doi.org/10.1016/j.csite.2026.107774.

Data availability

Data will be made available on request.

References

[1] E. Deniz, S. Çınar, Energy, exergy, economic and environmental (4E) analysis of a solar desalination system with humidification-dehumidification, Energy Convers. Manag. 126 (Oct. 2016) 12–19, https://doi.org/10.1016/j.enconman.2016.07.064.

[2] W. Wang, et al., Simultaneous production of fresh water and electricity via multistage solar photovoltaic membrane distillation, Nat. Commun. 10 (1) (Dec. 2019), https://doi.org/10.1038/s41467-019-10817-6.

[3] Q. Guo, et al., Enhancement and Optimization of Membrane Distillation Processes: a Systematic Review of Influential Mechanisms, Optimization and Applications, Elsevier B.V., Oct. 01, 2024, https://doi.org/10.1016/j.desal.2024.117862.

[4] E. Jones, M. Qadir, M.T.H. van Vliet, V. Smakhtin, S. mu Kang, The State of Desalination and Brine Production: a Global Outlook, Elsevier B.V., Mar. 20, 2019, https://doi.org/10.1016/j.scitotenv.2018.12.076.

[5] N. Ghaffour, S. Soukane, J.G. Lee, Y. Kim, A. Alpatova, Membrane Distillation Hybrids for Water Production and Energy Efficiency Enhancement: a Critical Review, Elsevier Ltd., Nov. 15, 2019, https://doi.org/10.1016/j.apenergy.2019.113698.

[6] S. Soukane, et al., Materials for Energy Conversion in Membrane Distillation Localized Heating: Review, Analysis and Future Perspectives of a Paradigm Shift, Elsevier Ltd., Oct. 01, 2022, https://doi.org/10.1016/j.rser.2022.112702.

[7] M.A.H. Mudhafar, Evaluation of a novel high-performance HP-HDH desalination system integrated with PV module and electrolyzer for fresh water and hydrogen productions, Renew. Energy 255 (Dec. 2025), https://doi.org/10.1016/j.renene.2025.123738.

[8] M. Ziauddin, F. Alnaimat, B. Mathew, Solar humidification and dehumidification system: integrating ultrasonic atomizer and solar still state-of-art, Sep. Purif. Technol. 378 (Dec) (2025), https://doi.org/10.1016/j.seppur.2025.134550.

[9] S. Al-Obaidani, E. Curcio, F. Macedonio, G. Di Profio, H. Al-Hinai, E. Drioli, Potential of membrane distillation in seawater desalination: thermal efficiency, sensitivity study and cost estimation, J. Membr. Sci. 323 (1) (Oct. 2008) 85–98, https://doi.org/10.1016/j.memsci.2008.06.006.

[10] A. Luo, N. Lior, Critical review of membrane distillation performance criteria, Desalination Water Treat. 57 (43) (Sep. 2016) 20093–20140, https://doi.org/10.1080/19443994.2016.1152637.

[11] J. Wu, E.M. Hoek, Current Opportunities and Challenges in Membrane-based Brine Management, Elsevier Ltd., Mar. 01, 2025, https://doi.org/10.1016/j.coche.2024.101079.

[12] Y.D. Kim, K. Thu, S.H. Choi, Solar-assisted multi-stage vacuum membrane distillation system with heat recovery unit, Desalination 367 (Jul. 2015) 161–171, https://doi.org/10.1016/j.desal.2015.04.003.

[13] A. Deshmukh, M. Elimelech, Understanding the impact of membrane properties and transport phenomena on the energetic performance of membrane distillation desalination, J. Membr. Sci. 539 (2017) 458–474, https://doi.org/10.1016/j.memsci.2017.05.017.

[14] R. Schwantes, Y. Morales, E. Pomp, J. Singer, K. Chavan, F. Saravia, Thermally driven ultrapure water production for water electrolysis – a techno-economic analysis of membrane distillation, Desalination 608 (Aug) (2025), https://doi.org/10.1016/j.desal.2025.118848.

[15] W. Zhao, et al., Membrane distillation for producing ultra-pure water for PEM electrolysis, Int. J. Hydrogen Energy 99 (Jan. 2025) 232–240, https://doi.org/10.1016/j.ijhydene.2024.12.219.

[16] T. Arthur, G.J. Millar, J. Love, Thermal management of water electrolysis using membrane distillation to produce pure water for hydrogen production, J. Water Process Eng. 67 (Nov. 2024), https://doi.org/10.1016/j.jwpe.2024.106255.

[17] P. Kumar, A. Date, N. Mahmood, R. Kumar Das, B. Shabani, Freshwater Supply for Hydrogen Production: an Underestimated Challenge, vol. 12, Elsevier Ltd., 2024, https://doi.org/10.1016/j.ijhydene.2024.06.257. Aug.

[18] C. Nellessen, T. Klein, H.J. Rapp, F. Rögener, Climate protection by membrane application – membrane distillation for the production of pharmaceutical ultrapure water, Chem. Ing. Tech. 93 (9) (Sep. 2021) 1345–1351, https://doi.org/10.1002/cite.202100030.

[19] "An Industrial Perspective on Ultrapure Water Production for Electrolysis.".

[20] A. Ali, F. Macedonio, E. Drioli, S. Aljlil, O.A. Alharbi, Experimental and theoretical evaluation of temperature polarization phenomenon in direct contact membrane distillation, Chem. Eng. Res. Des. 91 (10) (Oct. 2013) 1966–1977, https://doi.org/10.1016/j.cherd.2013.06.030.

[21] N. Sreedhar, N. Thomas, N. Ghaffour, H.A. Arafat, The Evolution of Feed Spacer Role in Membrane Applications for Desalination and Water Treatment: a Critical Review and Future Perspective, Elsevier B.V., May 15, 2023, https://doi.org/10.1016/j.desal.2023.116505.

[22] R. Rahmawati, et al., Engineered Spacers for Fouling Mitigation in Pressure Driven Membrane Processes: Progress and Projection, Elsevier Ltd., Oct. 01, 2021, https://doi.org/10.1016/j.jece.2021.106285.

[23] H.S. Abid, D.J. Johnson, R. Hashaikeh, N. Hilal, A Review of Efforts to Reduce Membrane Fouling by Control of Feed Spacer Characteristics, Elsevier B.V., 2017, https://doi.org/10.1016/j.desal.2017.07.019.

[24] E.H.C. Castillo, et al., 3D printed spacers for organic fouling mitigation in membrane distillation, J. Membr. Sci. 581 (Jul. 2019) 331–343, https://doi.org/10.1016/j.memsci.2019.03.040.

[25] S. Park, Y.D. Jeong, J.H. Lee, J. Kim, K. Jeong, K.H. Cho, 3D printed honeycomb-shaped feed channel spacer for membrane fouling mitigation in nanofiltration, J. Membr. Sci. 620 (Feb) (2021), https://doi.org/10.1016/j.memsci.2020.118665.

[26] A.A. Ibrahim, S. Leyer, From nature to engineering: bio-inspired spacer solutions for membrane distillation, Desalination 613 (Oct) (2025), https://doi.org/10.1016/j.desal.2025.119064.

[27] A.A. Ibrahim, M.A. Dalle, F. Janasz, S. Leyer, Novel spacer geometries for membrane distillation mixing enhancement, Desalination 580 (Jul. 2024), https://doi.org/10.1016/j.desal.2024.117513.

[28] G. Golubev, et al., Thin-film distillation coupled with membrane condenser for brine solutions concentration, Desalination 503 (May 2021), https://doi.org/10.1016/j.desal.2021.114956.

[29] R. Miladi, N. Frikha, A. Kheiri, S. Gabsi, Energetic performance analysis of seawater desalination with a solar membrane distillation, Energy Convers. Manag. 185 (Apr. 2019) 143–154, https://doi.org/10.1016/j.enconman.2019.02.011.

[30] M.R. Elmarghany, A.H. El-Shazly, M.S. Salem, M.N. Sabry, N. Nady, Thermal analysis evaluation of direct contact membrane distillation system, Case Stud. Therm. Eng. 13 (Mar) (2019), https://doi.org/10.1016/j.csite.2018.100377.

[31] H. Al-Sairfi, M.Z.A. Koshuriyan, M. Ahmed, Membrane distillation of saline feeds and produced water: a comparative study of an air-gap and vacuum-driven modules, Desalination Water Treat. 317 (Jan. 2024), https://doi.org/10.1016/j.dwt.2024.100145.

[32] S.M. Alawad, A.E. Khalifa, Performance and energy evaluation of compact multistage air gap membrane distillation system: an experimental investigation, Sep. Purif. Technol. 268 (Aug) (2021), https://doi.org/10.1016/j.seppur.2021.118594.

[33] H.C. Duong, P. Cooper, B. Nelemans, T.Y. Cath, L.D. Nghiem, Evaluating energy consumption of air gap membrane distillation for seawater desalination at pilot scale level, Sep. Purif. Technol. 166 (Jun. 2016) 55–62, https://doi.org/10.1016/j.seppur.2016.04.014.